ELSEVIER

Journal of Alloys and Compounds 239 (1996) 175–182

Journal of ALLOYS AND COMPOUNDS

Properties of $Zr(V_{0.25}Ni_{0.75})_2$ metal hydride as active electrode material

Andreas Züttel[a,*], Felix Meli[a], Daniel Chartouni[a], Louis Schlapbach[a], Frank Lichtenberg[b], Bernd Friedrich[c,1]

[a] *Institute of Physics, University of Fribourg, CH-1700 Fribourg, Switzerland*
[b] *Varta Batterie AG, R&D Center, Gundelhardtstrasse 72, D-65779 Kelkheim, Germany*
[c] *GFE, "Gesellschaft für Elektrometallurgie", Höfener Strasse 45, D-90431 Nürnberg, Germany*

Received 1 December 1995

Abstract

We have investigated the $Zr(V_xNi_{1-x})_2$ alloy series in the range of $0 \leq x \leq 0.4$ and observed very pronounced absorption and desorption properties in $Zr(V_{0.25}Ni_{0.75})_2$. We have shown previously that $Zr(V_{0.25}Ni_{0.75})_2$ has a high reversible capacity of 364 mA h g^{-1} (C/30 rate) and a good electrochemical cycle stability (8%/100 cycles capacity loss, C/3 rate). However, large-scale production of this alloy seems to be difficult, and annealing deteriorates the high capacity and the good kinetics as well. In this study we have analyzed the microstructure of the alloy and the thermodynamics of hydride formation of the alloy electrodes. Two different phases were observed, Zr_7Ni_{10} and $Zr(V_{0.33}Ni_{0.67})_{2.3}$; however, both of them are, as single phase alloys, not quite as good as their combination in $Zr(V_{0.25}Ni_{0.75})_2$.

Keywords: Metal hydride; Electrode; AB_2-alloys; Crystallography; XPS

1. Introduction

In previous work [1] we have shown that $Zr(V_{0.25}Ni_{0.75})_2$ is the most favorable alloy for use as a negative electrode in the $Zr(V_xNi_{1-x})_2$ $(0 \leq x \leq 0.6)$ system. This alloy showed a maximum reversible capacity of 364 mA h g^{-1} (10 mA g^{-1} discharge current) and very good kinetics for hydrogen adsorption and desorption in the electrolyte, i.e. the high-rate dischargeability (capacity measured in a 3 h discharge divided by the capacity measured in a 30 h discharge) is 82% [2]. There are only a very few corrosion resistant metal hydride alloys known which show electrochemically reversible capacities higher than 360 mA h g^{-1}. Moriwaki et al. [3] observed a discharge capacity of 366 mA h g^{-1} (value taken from figure) at a 50 mA g^{-1} discharge current on a $ZrMn_{0.5}Cr_{0.2}V_{0.1}Ni_{1.2}$ alloy (crystal structure: C15, lattice constant $a = 7.067$ Å, not single phase) and a capacity of 405 mA h g^{-1} (calculated from p–c–T isotherms) in the gas phase. Sawa and Wakao [4] studied hyper-stoichiometric alloys of the composition $Zr(V_{0.33}Ni_{0.67})_{2+\alpha}$ in the range of $0 \leq \alpha \leq 1$. They observed a slight increase of the discharge capacity in the range $0 \leq \alpha \leq 0.4$; however, the calculation of the number of interstitial sites as well as the experimental data showed a decrease of the hydrogen capacity with increasing $\alpha \geq 0.4$. Measured discharge capacities for $Zr(V_{0.33}Ni_{0.67})_{2+\alpha}$ were 297 mA h g^{-1} for $\alpha = 0$ and 311 mA h g^{-1} for $\alpha = 0.4$ respectively. $Zr(V_{0.33}Ni_{0.67})_{2.4}$ (C15 Laves phase) has a lattice constant of 7.048 Å and $\Delta H^0 = 24.89$ kJ mol_H^{-1} and $\Delta S^0 = -69.39$ J K^{-1} mol_H^{-1}, while for $Zr(V_{0.33}Ni_{0.67})_2$ a lattice constant of 7.102 Å and $\Delta H^0 = 29.24$ kJ mol_H^{-1} and $\Delta S^0 = -72.09$ J K^{-1} mol_H^{-1} was observed. Wakao et al. [5] also reported for $Zr(V_{0.33}Ni_{0.5}Mn_{0.17})_{2.4}$ a discharge capacity of 366 mA h g^{-1}, and $\Delta H^0 = 26.6$ kJ mol_H^{-1} and $\Delta S^0 = -70.4$ J K^{-1} mol_H^{-1}.

This paper reports the results of an intensive study

* Corresponding author. Tel.: (+41) 37 299 086; fax: (+41) 299 747; e-mail: Andreas.Zuettel@unifr.ch.

[1] Present address: Varta Batterie AG, Dieckstrasse 42, D-58089 Hagen, Germany.

PII S0925-8388(96)02259-1

of the properties of $Zr(V_{0.25}Ni_{0.75})_2$ as an active electrode material with a very high reversible capacity. The relation between electrode performance and the bulk- and surface-structure of the alloy is shown.

2. Experimental

2.1. Alloy preparation

The $Zr(V_{0.25}Ni_{0.75})_2$ alloy sample (6 g, ca. 1 cm^3, $M = 204.73$ g mol^{-1}) was prepared by r.f. levitation melting of the appropriate amounts of the elements, i.e. zirconium $m(Zr) = 2.6735$ g from Goodfellow UK, 99.8% Zr, vanadium $m(V) = 0.7465$ g from Koch-Light UK, 99.7% V, and nickel $m(Ni) = 2.5800$ g from Johnson Matthey UK, 99.99% Ni. Two other samples $Zr(V_{0.25}Ni_{0.75})_{2.3}$ and Zr_7Ni_{10} were prepared using the appropriate amounts of the elements.

The elements were cut and cleaned of oxides with a file. The weight was adjusted on a single piece of every element by removing the relevant amount with a file. The metals were then washed in acetone and subsequently introduced in the vacuum (10^{-7} mbar) of the r.f. levitation oven. A copper crucible was used to hold the metals together before power was applied and levitation occurred. The metals were initially heated up to 1480°C and they formed a homogeneous-looking round ball. The power was reduced and the sample was held at 1350°C for 5 min. Thereafter, the power was switched off and the sample was quenched in contact with the water-cooled crucible to room temperature within seconds. We estimate the cooling rate to be in the order of 100°C s^{-1}. Half of the sample was hit with a hammer and cracked into smaller pieces, the main reason for this procedure was to produce fresh surfaces. These pieces were immediately introduced into a stainless steel reactor. Subsequently, the latter was evacuated (10^{-2} mbar) and then floated with hydrogen gas at room temperature (20°C) and 40 bar. After approximately 10 min the pressure in the cylinder started to decrease and the outer side of the cylinder became remarkably hot. The sample was left for about an hour for complete hydriding and then dehydrided under vacuum (10^{-2} mbar). The hydriding–dehydriding procedure was repeated three times before the sample was completely dehydrided in vacuum (10^{-2} mbar) at approximately 100°C.

Another sample of the same alloy was made on a much larger scale (ca. 1 kg). A fraction of the alloy was annealed. These samples were cracked mechanically down to a grain size of ca. 500 μm.

2.2. Alloy characterization

X-ray diffraction was performed with copper radiation (Cu Kα $\lambda = 1.5406$ Å). Channel width was set to $2\Theta = 0.1°$ and the angular resolution was found to be $2\Theta = 0.2°$ (FWHM). The count time was set to 1 min per channel, resulting in a maximum count rate of approximately 5000 counts for the main peak in the spectrum (1.5% error in the count rate).

2.3. Electrochemical tests

For the electrochemical measurements, approximately 25 mg of the alloy powder was mixed with copper powder (Merck p.a. less than 63 μm) under the open atmosphere in the weight ratio of 1:3 and cold pressed (500 MPa) to a pellet ($d = 7$ mm). The pellets were fixed with a cylindrical Teflon-clip on a nickel holder. The electrodes were charged and discharged electrochemically in 6 M KOH electrolyte in a cell open to the atmosphere. A nickel plate was used as counter electrode and potentials were referred to a mercury|mercury oxide electrode. The discharge cut-off potential was -0.6 V with respect to the $Hg|HgO|OH^-$ reference electrode. The electrodes were tested in a half-cell experiment with constant charge (5 mA, i.e. 200 mA g^{-1}) and discharge (2.5 mA, i.e. 100 mA g^{-1}) current. The cycle life experiments were carried out at temperatures of 20 and 40°C. Every 10 cycles, an additional discharge at one-tenth of the normal discharge current (10 mA g^{-1}) was carried out. The equilibrium potentials were measured in special cycles with charge and discharge pulses of approximately 8 mA h g^{-1} during the pause of the pulses (5 min).

2.4. Gas-phase measurements

During the activation procedure 2 g of the sample were hydrided and dehydrided with a constant hydrogen gas flow of 1 cm^3 g^{-1} min^{-1} in the pressure cell at temperatures of 40 and 80°C. The temperature was controlled with a water bath and the pressure was monitored every minute.

2.5. X-ray photoelectron spectroscopy (XPS) measurements

Copper-free pellets were prepared for XPS analysis by pressing only the alloy powder to a pellet. For the surface analysis, samples were rinsed with twice-distilled water, dried in air and subsequently introduced in the ultra high vacuum (less than 10^{-8} Pa base pressure, 10^{-7} Pa H_2 partial pressure after introducing the degassing samples) of the spectrometer. The surface concentration of the elements was analyzed with

XPS in a VG ESCALAB 5 spectrometer using Mg Kα radiation of 1253.6 eV (Au $4f_{7/2}$ at 84.0 eV, 1.7 eV FWHM). The measured surface composition is an average over an area of 0.2 cm^2 and a depth of 10–20 Å. The sputter depth profiles (Ar^+, 2 keV) were evaluated using a standard rate of 500 Å cm^2 min^{-1} mA^{-1} (4 Å min^{-1}) and are therefore only to a factor of two precise in depth, owing to the element specific sputtering rate and the analyzing depth. The most significant differences in the depth profiles are observed within the top 50–100 Å. As the probing depth of XPS is ca. 30Å and the depth resolution upon sputtering is 20–30 Å, the top layer cannot be probed in more detail.

3. Results and discussion

3.1. X-ray diffraction

The X-ray diffraction pattern of the small-scale sample of $Zr(V_{0.25}Ni_{0.75})_2$ is shown in Fig. 1(a). Peak positions, intensities, and Miller indices for the cubic C15-Laves phase (structure type: Cu_2Mg; space group: *Fd3m* (227)) are listed in Table 1. Three minor peaks could not be attributed to the C15-Laves phase. The lattice constant was found to be $a = 7.082 \pm 0.003$ Å. The same value was found on the large-scale, as-cast sample ($a = 7.09 \pm 0.01$ Å). The diffraction patterns for the small- and the large-scale samples are, within the accuracy of the measurement, identical. The diffraction pattern of the annealed large-scale sample showed a drastic decrease in the intensity of the three additional peaks which do not belong to the C15-phase.

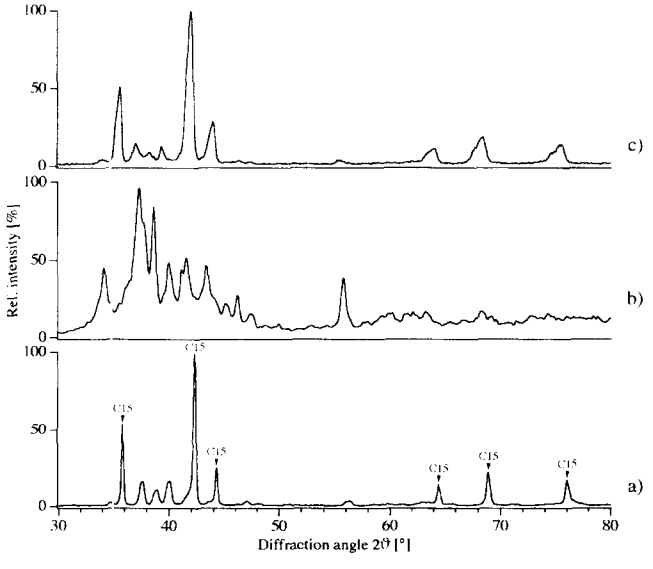

Fig. 1. X-ray diffraction pattern of (a) $Zr(V_{0.25}Ni_{0.75})_2$ sample (small-scale), (b) Zr_7Ni_{10}, and (c) $Zr(V_{0.33}Ni_{0.67})_{2.3}$.

Table 1
Peak position, intensity (relative peak height), Miller indices and *d* values of the $Zr(V_{0.25}Ni_{0.75})^2$ sample (small-scale) calculated from the X-ray diffraction pattern; the lattice constant for the cubic C15-Laves phase was found to be $a = 7.082 \pm 0.003$ Å

2ϑ (deg)	Intensity	*h k l*	*d* (Å)
35.7864	50	2 2 0	2.50713
37.5614	16		
38.8402	9		
39.9681	16		
42.2597	100	3 1 1	2.13685
44.2476	24	2 2 2	2.04535
64.4455	12	4 2 2	1.44464
68.8961	20	5 1 1	1.36177
76.0459	14	4 4 0	1.25053

The chemical analysis (inductive coupled plasma (ICP)) showed a slightly hyper-stoichiometric composition for the small-scale sample $Zr(V_{0.19}Ni_{0.81})_{2.12}$ and the nominal composition for the large-scale sample $(Zr(V_{0.25}Ni_{0.75})_{2.09}$.

3.2. Scanning electron microscope (SEM) and energy dispersive X-ray emission (EDX) analysis

Fig. 2 shows the SEM picture of a polished sample of $Zr(V_{0.25}Ni_{0.75})_2$. The EDX analysis in Table 2 of the two different intense regions in the SEM picture shows

Fig. 2. SEM picture of the $Zr(V_{0.25}Ni_{0.75})_2$ sample (small-scale). The two different phases were identified by EDX analysis; the dark phase is $Zr(V_{0.33}Ni_{0.67})_{2.3}$ and the lighter phase is Zr_7Ni_{10}.

Table 2
EDX analysis of the two different phases shown in Fig. 2

Phase	Element	At. %	Composition
Light gray	Zr	30.41	
	V	22.50	$Zr(V_{0.33}Ni_{0.67})_{2.3}$
	Ni	47.09	
Dark	Zr	39.73	
	V	2.78	Zr_7Ni_{10}
	Ni	57.49	

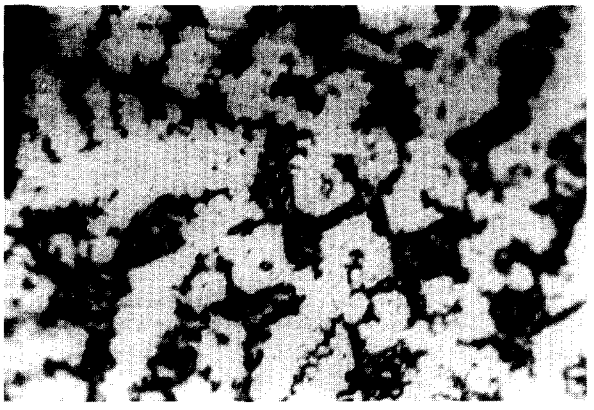

Fig. 3. Optical microscopy picture of a polished and etched (10% HCl, 1 min) lump of the $Zr(V_{0.25}Ni_{0.75})_2$ sample.

two different compositions, $Zr(V_{0.33}Ni_{0.67})_{2.3}$ for the gray region and Zr_7Ni_{10} for the darker region. Fig. 3 shows an optical microscopy picture of a polished and etched (10% hydrochloric acid, 1 min) lump of the $Zr(V_{0.25}Ni_{0.75})_2$ sample. The two identified phases were reproduced as single phase samples of the composition Zr_7Ni_{10} and $Zr(V_{0.33}Ni_{0.67})_{2.3}$ with the above-described procedure. X-ray diffraction patterns of these two alloys Zr_7Ni_{10} and $Zr(V_{0.33}Ni_{0.67})_{2.3}$ are shown in Figs. 1(b) and 1(c) respectively. For Zr_7Ni_{10} two orthorhombic phases are described in the literature [6], the so-called stoichiometric phase (space group *Pbca* (61); $a = 12.497(4)$ Å, $b = 9.210(8)$ Å, $c = 9.325(2)$ Å; density, $D = 7.68$ g cm^{-3}) and a so-called zirconium-rich phase (space group *Aba*2 (41); $a = 9.211(5)$ Å, $b = 9.156(8)$ Å, $c = 12.386(6)$ Å; density, $D = 7.78$ g cm^{-3}). These data were used to calculate [7] the diffraction pattern shown in Table 3 for the stoichiometric phase of Zr_7Ni_{10} and in Table 4 for the zirconium-rich phase of Zr_7Ni_{10}. Comparing these data with the diffraction pattern shown in Fig. 1(b) allows the conclusion that the Zr_7Ni_{10} phase found in the $Zr(V_{0.25}Ni_{0.75})_2$ is mainly the zirconium-rich phase (space group *Aba*2 (41)) of Zr_7Ni_{10}. Table 5 contains the X-ray diffraction data for the $Zr(V_{0.33}Ni_{0.67})_{2.3}$ alloy, which forms the cubic C15 Laves phase with a lattice constant of $a = 7.150 \pm 0.003$ Å.

3.3. Electrochemical activation and cyclic behavior

The discharge capacities measured at low-rate current (10 mA g^{-1}) are shown in Fig. 4. The $Zr(V_{0.25}Ni_{0.75})_2$ small-scale sample shows the highest maximum capacity of 340 mA h g^{-1} after 30 cycles. The maximum capacity of the $Zr(V_{0.33}Ni_{0.67})_{2.3}$ alloy sample is approximately 10% smaller compared with the capacity of $Zr(V_{0.25}Ni_{0.75})_2$. The measured maximum capacity for the Zr_7Ni_{10} phase is 170 mA h g^{-1}. On the large-scale samples of $Zr(V_{0.25}Ni_{0.75})_2$, a slower activation rate and a slightly smaller capacity was observed. However, the capacity of the sample that was not annealed, was close to the capacity of the small-scale sample. The cycle life parameters for the

Table 3
Calculated peak positions and intensities for the so-called stoichiometric phase of Zr_7Ni_{10} (space group *Pbca* (61): $a = 12.497(4)$ Å, $b = 9.210(8)$ Å, $c = 9.325(2)$ Å; density D = 7.68 g/cm^3

2ϑ (deg)	d (Å)	$h\,k\,l$	Intensity (%)
15.30	6.1930	0 0 2	55
24.08	3.6956	2 0 2	20
24.18	3.6814	0 2 2	22
28.83	3.0965	0 0 4	23
31.10	2.8756	2 2 2	16
31.57	2.8338	3 1 1	11
34.91	2.5697	2 0 4	26
37.81	2.3791	3 1 3	30
37.94	2.3715	1 3 3	81
38.91	2.3145	1 1 5	15
39.12	2.3028	4 0 0	34
39.36	2.2890	0 4 0	31
40.24	2.2408	2 2 4	100
41.07	2.1978	4 1 1	13
41.85	2.1584	4 0 2	25
42.08	2.1470	0 4 2	30
42.39	2.1322	3 3 1	18
43.86	2.0643	0 0 6	15
47.42	1.9171	3 3 3	10
56.70	1.6234	4 4 0	20
63.10	1.4733	5 3 3	11

Table 4
Calculated peak positions and intensities for the so-called zirconium-rich phase of Zr_7Ni_{10} (space group *Aba*2 (41): $a = 9.211(5)$ Å, $b = 9.156(8)$ Å, $c = 12.386(1)$ Å; density D = 7.78 g/cm^3)

2ϑ (deg)	d (Å)	$h\,k\,l$	Intensity (%)
23.81	3.7368	2 0 2	19
34.56	2.5954	4 0 2	47
37.39	2.4048	3 1 3	96
37.65	2.3889	3 3 1	100
38.62	2.3312	0 0 4	43
39.12	2.3025	0 4 0	42
39.87	2.2610	4 2 2	92
40.35	2.2354	0 4 1	18
40.56	2.2239	1 1 4	21
41.34	2.1842	2 0 4	25
41.35	2.1836	3 3 2	12
41.81	2.1605	2 4 0	29
41.99	2.1516	1 3 3	42
43.45	2.0828	6 0 0	31
45.71	1.9850	6 1 1	11
46.32	1.9603	2 4 2	11
46.97	1.9344	3 3 3	31
47.83	1.9017	6 0 2	13
47.94	1.8977	6 2 0	10
56.14	1.6382	0 4 4	27

Table 5
Peak position, intensity (relative peak height), Miller indices and d values of the $Zr(V_{0.33}Ni_{0.67})_{2.3}$ sample calculated from the X-ray diffraction pattern: the lattice constant for the cubic C15-Laves phase was found to be $a = 7.150 \pm 0.003$Å

2ϑ	Intensity	$h\,k\,l$	d(Å)
35.4453	51	2 2 0	2.53047
37.0303	9		
38.1856	4		
39.3440	8		
41.8428	100	3 1 1	2.15718
43.8091	29	2 2 2	2.0648
63.7662	11	4 2 2	1.45838
68.1773	18	5 1 1	1.37437
75.2534	14	4 4 0	1.26172

Table 6
Cycle life parameters of the $Zr(V_{0.25}Ni_{0.75})_2$ electrode at 20 °C and at 40 °C. C_{tot} is the maximum discharge capacity of the electrode, C_a^0 is the initial discharge capacity (at cycle 0), λ_{act} is the activation constant, and λ_{ox} is the oxidation constant; the discharge current was 100 mA g^{-1} (C/3) and the cut-off potential was set to −0.6 V vs. the Hg|HgO reference electrode

Temperature (°C)	C_{tot} (mA h g^{-1})	C_0a (mA h g^{-1})	λ_{act} (%/cycle)	λ_{ox} (%/cycle)
25	278	−147	12.9	0.083
40	295	−382	61	0.27

$Zr(V_{0.25}Ni_{0.75})_2$ electrode at 20°C and at 40°C are listed in Table 6. These parameters were calculated using our previously published cycle life model [8]. Increasing the cell temperature leads to a drastic increase of the oxidation constant, which means that the electrode corrodes in a cell at 40°C almost four times faster (27%/100 cycles) compared with an electrode at 20°C (8.3%/100 cycles).

The high-rate dischargeability was taken as a measurement of the kinetics of the electrodes. High-rate dischargeability is, in our case, defined as the ratio of the capacity measured in a 30 h discharge divided by the capacity measured in a 3 h discharge. The high-rate dischargeabilities for the different samples are shown in Fig. 5. The $Zr(V_{0.25}Ni_{0.75})_2$ small-scale sample shows the highest high-rate dischargeability of almost 80%, while Zr_7Ni_{10} shows the smallest at less than 20%. Also, the $Zr(V_{0.33}Ni_{0.67})_{2.3}$ alloy sample shows a lower rate capability than the $Zr(V_{0.25}Ni_{0.75})_2$ small-scale sample.

The electrochemically-measured absorption and desorption equilibrium curve of the $Zr(V_{0.25}Ni_{0.75})_2$ small-scale sample is shown in Fig. 6. The absorption curve shows two flat regions, while the desorption curve consists only of one plateau. This is even more pronounced in the calculated density of states (DoS) curves, i.e. density of energy-states for hydrogen in the host metal [9], which shows two peaks for absorption but only one for desorption. This behavior was also observed at the elevated temperature (40°C). These two different adsorption peaks could be assigned to the two different phases. The fact, that there was only one discharge peak observed may be explained by the very bad kinetics of the Zr_7Ni_{10} phase. Absorption occurs first on the sites with a higher binding energy and good kinetics, i.e. at a low pressure, followed by the occupation of the sites with a lower binding energy

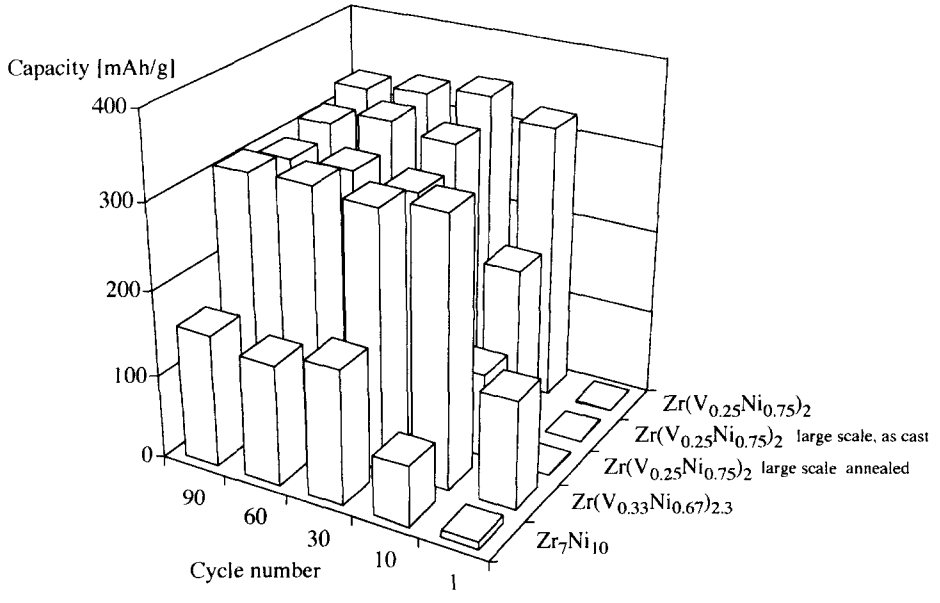

Fig. 4. Discharge capacities as a function of cycle number measured at low-rate current (10 mA g^{-1}) for the small-scale $Zr(V_{0.25}Ni_{0.75})_2$, large-scale as-cast $Zr(V_{0.25}Ni_{0.75})_2$, large-scale annealed $Zr(V_{0.25}Ni_{0.75})_2$, $Zr(V_{0.33}Ni_{0.67})_{2.3}$ and Zr_7Ni_{10} samples.

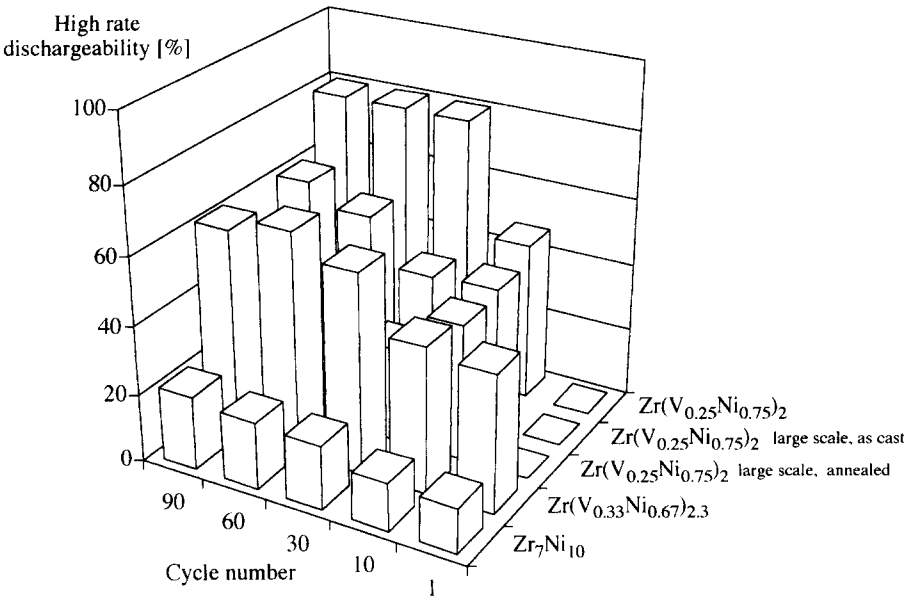

Fig. 5. High-rate dischargeabilities as a function of cycle number for the small-scale $Zr(V_{0.25}Ni_{0.75})_2$, large-scale as-cast $Zr(V_{0.25}Ni_{0.75})_2$, large-scale annealed $Zr(V_{0.25}Ni_{0.75})_2$, $Zr(V_{0.33}Ni_{0.67})_{2.3}$ and Zr_7Ni_{10} samples.

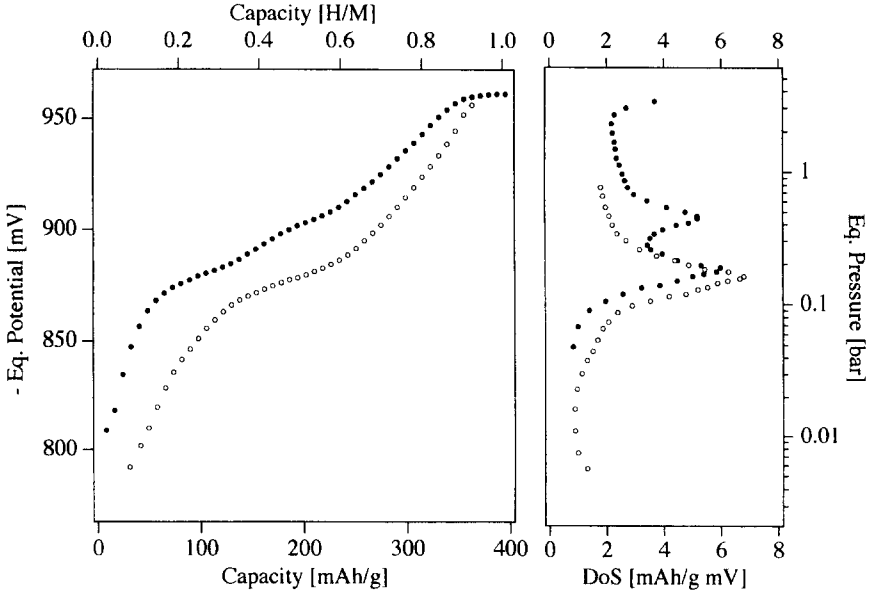

Fig. 6. Electrochemically-measured absorption and desorption equilibrium curve of the $Zr(V_{0.25}Ni_{0.75})_2$ small-scale sample at 20°C (left-hand side) and the calculated DoS curve (right-hand side).

and poor kinetics, i.e. at higher pressure. The desorption initially occurs on the sites with a higher binding energy due to the poor kinetics of the sites with lower binding energy. This makes the discharge curve fuzzy and leads to a non-equilibrium measurement.

3.4. Comparison of electrochemical and gas-phase charge–discharge behavior

A direct comparison of the electrochemically-measured charge–discharge equilibrium curve with the gas-phase measurement is shown in Fig. 7. The measuring range is much larger in the electrochemical case. However, in the common part of the curve, the electrochemical and the gas-phase data fit very well together. Furthermore, the electrochemical measurement of the equilibrium curve seems to be more sensitive and shows the details more sharply. In order to determine the equilibrium pressures and potentials, the position of the peaks were obtained from the DoS curves and are listed in Table 7. The reaction enthalpy and entropy were calculated from the results of the electrochemical equilibrium-measurements at 20°C and 40°C according to the following equation:

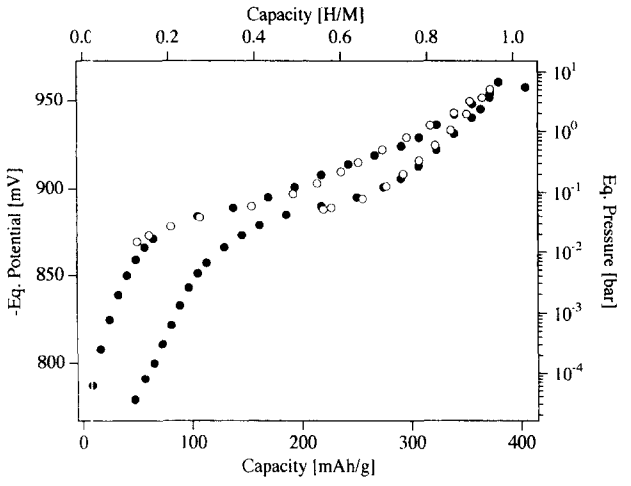

Fig. 7. Electrochemical (●) and gas-phase (○) absorption and desorption equilibrium curve of the $Zr(V_{0.25}Ni_{0.75})_2$ small-scale sample measured at a constant temperature of 40°C.

Table 7
Equilibrium potentials and pressures for absorption and desorption measured on the plateau (position of peak maximum in the DoS curve) of the $Zr(V_{0.25}Ni_{0.75})$ sample at different temperatures

	Potential (mV)		Pressure (bar)	
Temperature (°C)	Absorption	Desorption	Absorption	Desorption
20	882.0	878.0		
	905.5	–		
40	892.3	887.2	0.05	0.05
	920.6	–	1.3	–
80			0.3	0.22
			4.5	–

$$nF\Delta E^0 = \Delta H - T\Delta S$$

where ΔE^0 is the difference between the potential of the metal hydride electrode and the potential of the Hg|HgO reference electrode, F is the Faraday constant (96494 A s mol^{-1}), n is the number of electrons ($=1$), ΔH is the reaction enthalpy, ΔS the reaction entropy and T the absolute temperature. The potential of the Hg|HgO reference electrode is temperature dependent and given by the following equation [10]:

$$E^0_{Hg|HgO} = 1.18041 - [4.4666\times10^{-3} - 6.93606\times10^{-4}\ln(T)]T - 1.0788\times10^{-6}T^2 + 4.512\times10^{-10}T^3 - 5.232T^{-1}$$

The absorption enthalpy was found to be $\Delta H^0 = 22.8$ kJ mol_H^{-1} and the desorption enthalpy is $\Delta H^0 = 24.9$ kJ mol_H^{-1}, with $\Delta S^0 = -66.4$ J K^{-1} mol_H^{-1}. The enthalpy for the second absorption peak is $\Delta H^0 = 20.3$ kJ mol_H^{-1}.

The discharge capacities were found to be 360 mA h g^{-1} at 20°C and 380 mA h g^{-1} at 40°C. This is because of the higher equilibrium potential at 40°C, compared with 20°C, in combination with the constant end of discharge potential of −0.6 V.

3.5. Surface composition

The $Zr(V_{0.25}Ni_{0.75})_2$ electrode was analyzed in two different states of the cycle life curve in order to investigate the activation mechanism. The surface composition of the freshly-prepared electrode for the metallic elements zirconium, vanadium and nickel is shown in Fig. 8. The top layer of the alloy grains (30 Å) contains 75% zirconium oxide, 10% vanadium oxide and 15% metallic nickel. Below 30 Å the nickel concentration increases quickly to 50% of the alloy bulk concentration. At the same time, vanadium and zirconium adjust to their bulk concentration and become almost completely metallic.

During the electrochemical activation of the electrode (30 electrochemical cycles) the concentration of the elements in the surface changes drastically (Fig. 9). The zirconium oxide concentration in the top layer (30 Å) decreased to 30%, while the nickel concentration increased to 70% and most of the nickel became oxidized. The concentration of vanadium decreased to close to zero. The disappearance of vanadium can be

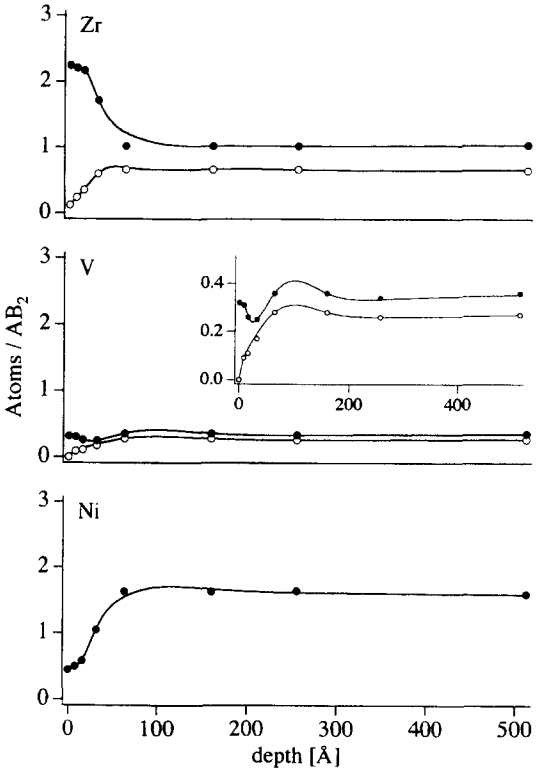

Fig. 8. XPS depth profile of Zr, V and Ni for the as-cast $Zr(V_{0.25}Ni_{0.75})_2$ small-scale sample: (●) represent the total amount of the element (metallic and oxidized state); (○) represent the metallic constituents of the elements in terms of atoms/AB_2, where AB_2 stands for the sum of Zr + V + Ni.

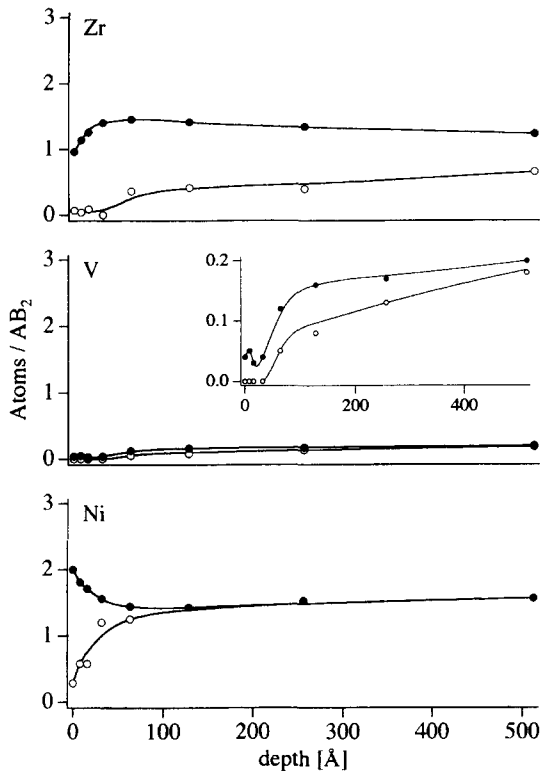

Fig. 9. XPS depth profile of Zr, V and Ni for the $Zr(V_{0.25}Ni_{0.75})_2$ small-scale sample after 30 electrochemical cycles: (●) represent the total amount of the element (metallic and oxidized state); (○) represent the metallic constituents of the elements in terms of atoms/AB_2, where AB_2 stands for the sum of Zr + V + Ni.

explained by the high solubility of vanadium (0.4 g l^{-1} in pure water [11] and even higher in alkaline solution) compared with the other elements in the alloy. The significant enrichment of nickel in the top surface layer compared with the freshly-prepared electrode, combined with the dissolution of vanadium oxide, is responsible for the activation of the electrode [2].

4. Conclusions

$Zr(V_{0.25}Ni_{0.75})_2$ is an intermetallic compound with a high discharge capacity (approximately 360 mA h g^{-1}) and is a simple composition of only three elements. However, the metallurgy seems to be quite complicated. The two-phase alloy has superior properties, i.e. higher discharge capacity and better kinetics, for use as an electrode material than the corresponding single-phase alloy. The two individual phases which could be identified, are, individually, both inferior in their properties compared with the combination of these phases in $Zr(V_{0.25}Ni_{0.75})_2$. The positive synergism of the two phases may be explained in different ways. Zr_7Ni_{10} is known to have a high capacity (H/M = 1, $C = 372$ mA h g^{-1}). However, its hydride is quite stable ($p_{eq} \approx 4 \times 10^{-2}$ bar at 25°C) [12] and the kinetics of this phase seems to be very poor. In contrast, $Zr(V_{0.33}Ni_{0.67})_{2.3}$, with better kinetics, may assist the system as a catalyst for hydrogen absorption and desorption.

Acknowledgment

Financial support by the Bundesamt für Energiewirtschaft BEW (Swiss Department of Energy) is acknowledged.

References

[1] A. Züttel, F. Meli and L. Schlapbach, *J. Alloys Comp., 203* (1994) 235.
[2] A. Züttel, F. Meli and L. Schlapbach, *J. Alloys Comp., 209* (1994) 99.
[3] Y. Moriwaki, T. Gamo, H. Seri and T. Iwaki, *J. Less-Common Met., 172–174* (1991) 1211.
[4] H. Sawa and S. Wakao, *Mater. Trans. JIM, 31* (6) (1990) 487.
[5] S. Wakao, H. Sawa and J. Furukawa, *J. Less-Common Met., 172–174* (1991) 1219.
[6] M.E. Kirkpatrick, J.F. Smith and W.L. Larsen, *Acta Crystallogr., 15* (1962) 894.
[7] K. Yvon, `lazy` and `pulverix`, Laboratoire de Cristallographie, Université de Genève, 24 Quai Ernest-Ansermet, Genève 4, Switzerland.
[8] A. Züttel, F. Meli and L. Schlapbach, *J. Alloys Comp., 200* (1993) 157.
[9] A. Züttel, F. Meli and L. Schlapbach, *J. Alloys Comp., 206* (1994) 31.
[10] J. Balej, *Int. J. Hydrogen Energy, 10* (6) (1985) 365.
[11] J. Meyer and M. Aulich, *Z. Anorg. Allg. Chem., 194* (1930) 278.
[12] J.M. Joubert, M. Latroche and A. Percheron-Guégan, J. Alloys Comp., in press.